



## **Final Draft of the original manuscript**

Jiang, P.; Blawert, C.; Scharnagl, N.; Bohlen, J.; Zheludkevich, M.:  
**Mechanistic understanding of the corrosion behavior of  
Mg<sub>4</sub>Zn<sub>0.2</sub>Sn alloys: from the perspective view of  
microstructure.**

In: Corrosion Science. Vol. 174 (2020) 108863.

First published online by Elsevier: 09..07.2020

<https://dx.doi.org/10.1016/j.corsci.2020.108863>

1 **Mechanistic understanding of the corrosion behavior of Mg<sub>4</sub>Zn<sub>0.2</sub>Sn alloys:**  
2 **from the perspective view of microstructure**

3 Pingli Jiang<sup>a\*</sup>, Carsten Blawert<sup>a</sup>, Nico Scharnagl<sup>a</sup>, Jan Bohlen<sup>a</sup>, Mikhail L. Zheludkevich<sup>a,b</sup>

4 <sup>a</sup> Magnesium Innovation Centre - MagIC, Institute of Materials Research, Helmholtz-Zentrum  
5 Geesthacht, Max-Planck Str.1, Geesthacht 21502, Germany

6 <sup>b</sup> Faculty of Engineering, University of Kiel, Kaiserstrasse 2, 24143 Kiel, Germany

7

8 \* Corresponding author:

9 Pingli Jiang, E-Mail: [pingli.jiang@hzg.de](mailto:pingli.jiang@hzg.de)

10

1 **Abstract**

2 The corrosion behavior of as-cast and extruded Mg<sub>4</sub>Zn<sub>0.2</sub>Sn (wt.%) alloys was  
3 comprehensively compared in 0.5 wt.% NaCl solution. Microstructure and surface chemistry  
4 related corrosion performance has been revealed. Zinc-supersaturated solid solution is formed  
5 around the intermetallics in the as-cast alloy, but zinc alternately segregates between the  $\alpha$ -Mg  
6 matrix in the extruded alloy. According to Scanning Kelvin Probe Force Microscopy and  
7 immersion tests, micro-galvanic corrosion between the precipitates (intermetallics or impurity  
8 particles) or Zinc-rich area and the matrix resulted in severe localized corrosion in both  
9 conditions. However, alternation of microstructure induced by extrusion significantly  
10 enhanced the corrosion resistance of Mg<sub>4</sub>Zn<sub>0.2</sub>Sn alloy.

11 **Keywords:** Magnesium alloy; tin; corrosion behavior; extrusion; micro-galvanic corrosion.

12

## 1 **1. Introduction**

2 Since the early 20th century, magnesium (Mg) alloys have been used in industrial applications  
3 as structural materials [1]. The lowest density, about a quarter that of steel and two-thirds that  
4 of aluminum, imparts great potential to the application of Mg alloys as light-weighting  
5 materials in the areas of aerospace, portable electronics and automotive. Reducing the weight  
6 of structural components can efficiently decrease the emission of CO<sub>2</sub> and improve the energy  
7 efficiency. However, the inadequate formability, ductility and corrosion resistance mainly limit  
8 the wide applications of Mg alloys [2, 3]. Up to now, many efforts have been made to improve  
9 those properties of Mg alloys, including thermo [4, 5] and mechanical [6, 7] processing or  
10 integrated thermo-mechanical processing [8], optimization of alloy composition [9-12], and  
11 use of alternative fabrication routes [13].

12 The magnesium-zinc (Mg-Zn) system has been paid more and more attention recently. Studies  
13 revealed that the corrosion resistance of Mg-Zn alloys can be enhanced with the increment of  
14 Zn content up to 5 wt.% due to the homogenous distribution of Zn, refined microstructure and  
15 the formation of more protective film on the surface [14-16]. However, much higher addition  
16 of Zn (> 5 wt.%) results in more and larger intermetallics, which decreases the corrosion  
17 resistance of the alloy due to the enhanced micro-galvanic corrosion, and also deteriorates the  
18 strength of the alloy because of the formation of more crack sources (intermetallics) [14].  
19 Therefore, it is suggested that 4 wt.% should be the limit of the Zn content in Mg to balance  
20 the corrosion rate and mechanical properties of Mg-Zn alloys [17].

21 For potential commercial applications, the corrosion resistance of Mg-Zn binary alloy are still  
22 not high enough to effectively prevent the deterioration of the alloys during service. Tin (Sn),  
23 as one of the further alloying elements, owns high overpotential for hydrogen evolution and  
24 thus has the potential to tailor the hydrogen release of Mg alloys [18]. The addition of Sn has  
25 been proven to adjust the corrosion and mechanical properties of Mg-Sn binary alloys via

1 variation of Mg<sub>2</sub>Sn phase content and the homogeneity of microstructure [19]. Furthermore,  
2 Jiang et al. [18, 20] reported that serious localized corrosion of Mg<sub>4</sub>Zn alloy was weakened by  
3 the addition of 1 wt.% or 1.5 wt.% Sn, whereas 2 wt.% Sn strongly deteriorated the corrosion  
4 properties of the alloy because of the high number of Mg<sub>2</sub>Sn intermetallics as pitting corrosion  
5 initiators. However, currently, studies about the Mg-Zn-Sn system are still limited, especially  
6 on the corrosion properties. Therefore, in this study, only a minor amount (0.2 wt.%) of Sn is  
7 added to the Mg<sub>4</sub>Zn (wt.%) base alloy aiming to obtain better corrosion performance by  
8 preventing the excessive formation of Mg<sub>2</sub>Sn phases.

9 Although the majority of current commercial Mg components are cast products, thermo-  
10 mechanical processed Mg alloys are attracting increasing attention from industry. For example,  
11 hot-extruded Mg alloys can be used in automotive interior, luggage, motorcycle and bicycle  
12 applications [21]. Due to the severe plastic deformation during hot extrusions, refinement of  
13 the microstructure, dynamic precipitation as well as the redistribution of alloying elements can  
14 be achieved. This can help to improve the corresponding corrosion resistance and mechanical  
15 properties of Mg alloys [1]. Therefore, hot extrusion is applied in this study aiming to improve  
16 the corrosion properties of Mg<sub>4</sub>Zn0.2Sn alloy.

17 In the present study, the corrosion behavior of as-cast and extruded Mg<sub>4</sub>Zn0.2Sn alloys is  
18 compared in 0.5 wt.% NaCl solution. The Volta potential difference between the second phases  
19 and the matrix as well as the corrosion morphologies after immersion tests were determined to  
20 understand the corrosion mechanisms of the alloy before and after extrusion.

## 21 **2. Experimental**

### 22 2.1 Material preparation

23 Nominal Mg<sub>4</sub>Zn0.2Sn (wt.%) alloy was prepared with pure Mg (99.9 %), Zn (99.995 %) and  
24 Sn (99.963 %) using an indirect chill casting procedure [22]. Billets with a diameter of 49 mm  
25 and a length of 150 mm were machined for indirect hot extrusion experiment of the alloy. The

1 temperature for the homogenization process before extrusion and for the extrusion process was  
2 320 °C and 375 °C, respectively, chosen according to the phase diagram of Mg<sub>4</sub>Zn-Sn system  
3 shown in Fig. 1. The homogenization process lasted for 24 h and was followed by quenching  
4 with warm water. A round bar with a diameter of 10 mm was extruded at 2.2 mm/s (ram speed).  
5 The chemical compositions of the as-cast and extruded Mg<sub>4</sub>Zn<sub>0.2</sub>Sn alloys were analyzed by  
6 spark optical emission spectroscopy (Spectrolab M9) and atomic absorption spectrometer  
7 (Agilent 240FS AA) (for the analysis of Sn), listed in Table 1.

## 8 2.2 Microstructure characterization

9 The specimens for microstructure analysis were firstly wet ground with silicon carbide papers  
10 from 800 to 2500 grit, and then polished in a mixture of 1 μm diamond suspension and oxide  
11 polishing suspension (OPS). For optical observation, the polished samples were etched using  
12 a picric acid-based etchant (150 mL ethanol, 20 mL deionized water, 6.5 mL acetic acid and 4  
13 - 5 g picric acid). Protective glasses and gloves are required when dealing with picric acid and  
14 the chromium trioxide (CrO<sub>3</sub>) solution mentioned later. After immersion in the etchant for  
15 about 10 s, the sample surface was rinsed with ethanol to stop the etching process and dried in  
16 an oil-free air stream. The optical images were utilized to calculate the average grain size using  
17 a linear intercept method by AnalySIS pro (version 5) software. The microstructures were also  
18 evaluated by scanning electron microscopy (SEM) (TESCAN Vega 3 SB). To facilitate the  
19 observation of second phases, the backscattering electron (BSE) mode was utilized and the  
20 compositions of the different phases in the alloys were determined by energy dispersive X-ray  
21 spectroscopy (EDS) (Eumex). The acceleration voltage was 20 kV.

## 22 2.3 Electrochemical measurements

23 The Volta potential differences between different constituents and the matrix were measured  
24 by scanning kelvin probe force microscopy (SKPFM) (JPK NanoWizard). Shortly before the  
25 SKPFM measurements, the samples were polished with 1 μm diamond suspension in OPS and

1 subsequently with single OPS. After ultrasonically cleaning in an ethanol bath, the specimens  
2 were dried in air and immediately transferred to the measurements. A chromium/platinum  
3 (Cr/Pt) coated silicon probe (Budget Sensors) with resonance frequency of 75 kHz and force  
4 constant of 3 N/m was utilized for the measurements. The Volta potential difference maps were  
5 obtained in a resolution of  $512 \times 512$  pixels with a hover height of 100 nm.  
6 Potentiodynamic polarization curves were collected in 0.5 wt.% sodium chloride (NaCl)  
7 solution after the samples were conditioned at open circuit potential (OCP) for 30 min and 48  
8 h, respectively. A conventional three-electrode cell was utilized, which consisted of a Pt mesh  
9 as auxiliary electrode, a silver/silver chloride (Ag/AgCl) electrode as reference electrode and  
10 the specimen as working electrode. Ground samples (until 1200 grit) with  $0.5 \text{ cm}^2$  exposed area  
11 were used for the measurements and the data was recorded from -150 mV vs. OCP using a Gill  
12 AC potentiostat at a scan rate of 0.2 mV/s at room temperature (air-conditioned at  $21 \pm 1 \text{ }^\circ\text{C}$ ).  
13 The obtained data was analyzed using ACM Analysis software (version 4) and only the  
14 cathodic branches were considered. At least three specimens were tested for statistic purpose  
15 (this also applies for the following hydrogen evolution and weight loss tests).

#### 16 2.4 Corrosion behavior investigation

17 To understand the corrosion mechanism of as-cast and extruded Mg<sub>4</sub>Zn<sub>0.2</sub>Sn alloys, two  
18 immersion tests for different durations were carried out in 0.5 wt.% NaCl solution. The first  
19 test was performed on polished samples for 6 h (short immersion). After immersion, the  
20 corroded surfaces were cleaned with 180 g/L chromium trioxide aqueous solution (chromic  
21 acid) and rinsed with deionized water and ethanol. SEM examination was performed to  
22 determine the role of each constituent in the alloy during immersion. Only polished specimens  
23 were used to check the possible risk of removal of second phases due to the cleaning process  
24 in chromic acid. No removal of material was observed on those sample surfaces. The second  
25 test with extended immersion period was performed on ground specimens for 48 h to study the

1 surface and cross-sectional morphologies after corrosion. Elemental distribution in the cross  
2 sections of the corrosion product layers was determined by EDS element mapping. The  
3 mapping was performed at a resolution of  $191 \times 256$  pixels and 80 ms for each pixel. The  
4 surface in the transverse direction (perpendicular to the extrusion direction) of extruded  
5 Mg<sub>4</sub>Zn<sub>0.2</sub>Sn alloy was used for both immersion tests and the aforementioned potentiodynamic  
6 polarization measurements.

7 Hydrogen evolution and weight loss tests were performed to determine the corrosion rates (*CR*)  
8 of as-cast and extruded Mg<sub>4</sub>Zn<sub>0.2</sub>Sn alloys in 0.5 wt.% NaCl solution. The evolved hydrogen  
9 was collected using an inverted funnel and burette. After 168 h, the corrosion products were  
10 removed with chromic acid solution and the weight changes of the samples were measured.

### 11 **3. Results**

#### 12 3.1 Microstructure analysis

13 Fig. 2 displays the OM images showing the microstructures of as-cast and extruded  
14 Mg<sub>4</sub>Zn<sub>0.2</sub>Sn alloys. Apparently, the as-cast Mg<sub>4</sub>Zn<sub>0.2</sub>Sn alloy reveals a coarse dendritic  
15 microstructure while the extruded Mg<sub>4</sub>Zn<sub>0.2</sub>Sn alloy exhibits significantly refined globular  
16 grains. The average grain sizes are  $232 \pm 20$   $\mu\text{m}$  and  $34 \pm 1$   $\mu\text{m}$  for as-cast and extruded  
17 Mg<sub>4</sub>Zn<sub>0.2</sub>Sn alloys respectively, demonstrating that the extrusion process greatly refines the  
18 microstructure of the alloy.

19 According to Figs. 3a and 3b, divorced eutectic compounds in irregular and circular shapes are  
20 formed in the microstructure of as-cast Mg<sub>4</sub>Zn<sub>0.2</sub>Sn alloy. The morphologies of the eutectic  
21 phases are similar to those reported in as-cast Mg<sub>4</sub>Zn<sub>1</sub>Sn alloy [11]. Those micron-sized  
22 particles are distributed in the interdendritic regions. Moreover, the brighter contrast of the  
23 particle-free interdendritic regions indicates segregation of heavier elements at those places,  
24 which is consistent with enrichment of the remaining melt with Zn and Sn during solidification  
25 process. For extruded Mg<sub>4</sub>Zn<sub>0.2</sub>Sn alloy (Figs. 3c, 3d, 3e and 3f), those large particles

1 disappear after extrusion and sub-micron-scale precipitates are visible instead, which are  
2 mainly distributed at the grain boundaries. Similar microstructures of extruded Mg<sub>4</sub>Zn-Sn  
3 alloys were also revealed in reference [20]. However, a few larger particles (Fig. 3f) in  
4 polygonal shapes can also be revealed. Bright globular particles exist inside some of those  
5 polygonal particles. It is noticed that there are alternating bright and dark regions or bands in  
6 the microstructure of extruded Mg<sub>4</sub>Zn<sub>0.2</sub>Sn alloy, which are especially obvious in the  
7 transverse direction (Fig. 3e).

8 The phase compositions of as-cast and extruded Mg<sub>4</sub>Zn<sub>0.2</sub>Sn alloys were also determined by  
9 XRD (the XRD results are not shown here). However, only  $\alpha$ -Mg phase was detected. The  
10 absence of possible Mg-Zn or Mg-Sn binary phases may be explained by the detection  
11 limitation of the instrument. Therefore, EDS was used to study the phase constituents in as-  
12 cast and extruded Mg<sub>4</sub>Zn<sub>0.2</sub>Sn alloys. As marked in Fig. 3b, letters A - C represent the second  
13 phases, brighter precipitate-free interdendritic regions and grey  $\alpha$ -Mg dendrites in as-cast  
14 Mg<sub>4</sub>Zn<sub>0.2</sub>Sn alloy. In Figs. 3d and 3f, letters D - H refer to the darker matrix region, brighter  
15 matrix region, tiny particles, grey polygonal part (or single grey polygonal particles) and bright  
16 globular part of the larger particles in extruded alloy, respectively. At least ten sites were  
17 analyzed by EDS and the average compositions of the different phases are shown in Table 2  
18 and Table 3. It is revealed that the compositions of the irregular and circular eutectic second  
19 phases in as-cast Mg<sub>4</sub>Zn<sub>0.2</sub>Zn alloy are similar. Those phases are rich in Mg and Zn with a  
20 very small amount of Sn, indicating that they are Mg-Zn binary phases. According to the atomic  
21 percentage composition, it seems that those second phases are Mg<sub>7</sub>Zn<sub>3</sub>. However, due to the  
22 contribution of the  $\alpha$ -Mg in the eutectic phase ( $\alpha$ -Mg + Mg-Zn phase) and the underlying  $\alpha$ -  
23 Mg matrix, the real concentration of Mg in the second phase analyzed by EDS can be largely  
24 affected. Based on the EDS and XRD results reported by Cai et al. [14], those Mg-Zn binary  
25 phases should be MgZn phases, which are formed by the decomposition of Mg<sub>7</sub>Zn<sub>3</sub> phases at

1 the eutectic temperature (325 °C). Similar results have also been reported in other studies. [15,  
2 23, 24]. Herein, the Mg-Zn binary phases formed in the studied as-cast Mg<sub>4</sub>Zn<sub>0.2</sub>Sn alloy will  
3 be simply referred as Mg<sub>x</sub>Zn<sub>y</sub> phases. As expected, a much higher content of Zn is detected in  
4 the brighter second phase-free interdendritic regions compared to the grey matrix dendrites. In  
5 the case of extruded Mg<sub>4</sub>Zn<sub>0.2</sub>Sn alloy, the difference of Zn content between the darker and  
6 brighter matrix regions is not so significant but the Zn content is still slightly higher in the  
7 brighter regions. For the tiny particles, considering such a small size, it is difficult to define the  
8 exact or even approximate composition by EDS. However, compared to Sn, the relatively  
9 higher amount of Zn may suggest that they are Mg-Zn phases (hereafter also referred as  
10 Mg<sub>x</sub>Zn<sub>y</sub> phases) (more evidence is found in the element distribution of the cross sections after  
11 immersion tests). For the grey polygonal parts/particles, in comparison with Zn and Sn, much  
12 higher amount of Si was detected, which should be Mg<sub>2</sub>Si phases. Because no ternary Mg-Sn-  
13 Si or Mg-Zn-Si can be formed [25-27]. Compared with the grey polygonal parts/particles, those  
14 bright globular parts inside the grey polygonal particles contain a similar amount of Zn, Sn and  
15 silicon (Si). However, the content of iron (Fe) and manganese (Mn) is evident, suggesting that  
16 they are Fe-Mn impurities. Furthermore, element mapping was recorded to confirm the element  
17 distribution in the microstructures of both Mg<sub>4</sub>Zn<sub>0.2</sub>Sn alloys, as shown in Fig. 4. This is  
18 especially important considering the different element compositions of the darker and brighter  
19 matrix regions of the extruded alloy. The EDS mapping results correlate well with the EDS  
20 analysis. As expected, those impurity elements (Si, Fe and Mn) enrich inside the second phases  
21 in the as-cast Mg<sub>4</sub>Zn<sub>0.2</sub>Sn alloy. For the extruded alloy, an obviously alternating distribution  
22 of Mg and Zn in the corresponding darker and brighter regions is observed, indicating that  
23 segregation of Zn still exists in the alloy after extrusion. Moreover, the existence of those Mg<sub>2</sub>Si  
24 phases and Fe-Mn/Mg<sub>2</sub>Si co-exited precipitates are also confirmed.

### 25 3.2 Corrosion performance

### 1 3.2.1 SKPFM measurement

2 To facilitate the understanding of the corrosion behavior of Mg<sub>4</sub>Zn<sub>0.2</sub>Sn alloy and the  
3 influence of different microstructure, the distribution of surface Volta potential difference over  
4 different constituents of the as-cast alloy was measured by SKPFM, as shown in Fig. 5.  
5 Obviously, according to Fig. 5b, the divorced Mg<sub>x</sub>Zn<sub>y</sub> phases exhibit higher Volta potential  
6 compared with the surrounding matrix. The average Volta potential difference between the  
7 Mg<sub>x</sub>Zn<sub>y</sub> phase and the matrix is  $86 \pm 26$  mV. Interestingly, slightly higher Volta potential can  
8 be noted also for the matrix surrounding the second phases when compared with the matrix  
9 that is a bit further away from the second phases. Combining the SKPFM results with the  
10 microstructure of as-cast Mg<sub>4</sub>Zn<sub>0.2</sub>Sn alloy, the matrix around the Mg<sub>x</sub>Zn<sub>y</sub> phase should be  
11 those Zn-rich interdendritic regions. Therefore, the Mg<sub>x</sub>Zn<sub>y</sub> phases possess the highest nobility,  
12 followed by the Zn-rich interdendritic regions and the  $\alpha$ -Mg dendrites (matrix) respectively.  
13 Accordingly, from kinetic interpretations, galvanic couples can be formed between Mg<sub>x</sub>Zn<sub>y</sub>  
14 intermetallic as possible cathode with both intermetallic-free regions (Zn-rich interdendritic  
15 region and  $\alpha$ -Mg matrix) as possible anode and between Zn-rich interdendritic area (cathode)  
16 and  $\alpha$ -Mg matrix (anode) when the alloy is immersed in corrosive electrolyte.  
17 The extremely fine second phases (sub-micron-scale) in extruded Mg<sub>4</sub>Zn<sub>0.2</sub>Sn alloy and the  
18 low content and small size (about 3  $\mu$ m) of those impurity particles pose great difficulty to the  
19 successful SKPFM measurement of a desired position (place with impurity particle).  
20 Nevertheless, it has been widely accepted that a Fe-containing impurity particle plays a critical  
21 role in the corrosion performance of Mg alloys when exposed to corrosive environment [28].  
22 Moreover, Fe-containing impurity particles possess much higher standard electrode potential  
23 than Mg and the high Volta potential difference between an Fe-containing impurity particle  
24 and  $\alpha$ -Mg matrix has also been determined in pure Mg in refs. [29-31]. Thus, it can be  
25 speculated that galvanic coupling may be formed between the Fe-Mn/Mg<sub>2</sub>Si co-existed particle

1 and the surrounded  $\alpha$ -Mg matrix besides the  $Mg_xZn_y$  phases when the extruded  $Mg_4Zn_{0.2}Sn$   
2 alloy is exposed to corrosive electrolyte. However, the presence of Mn can suppress the  
3 detrimental effect of Fe on the corrosion behavior of Mg alloys. Therefore, the relative galvanic  
4 activity of the couple between the Fe-Mn/ $Mg_2Si$  particle and the matrix and that between the  
5 tiny second phase and the matrix has to be considered.

### 6 3.2.2 Short-term immersion

7 The respective role of each phase in both as-cast and extruded  $Mg_4Zn_{0.2}Sn$  alloys is revealed  
8 during the corrosion process. Short immersion tests (6 h) in 0.5 wt.% NaCl solution were  
9 conducted on polished alloy surfaces and the corrosion products were removed with chromic  
10 acid, as displayed in Fig. 6. For as-cast  $Mg_4Zn_{0.2}Sn$  alloy (Figs. 6a and 6b), the  $\alpha$ -Mg dendrites  
11 and the  $\alpha$ -Mg inside the eutectic phase dissolve preferentially, while the  $Mg_xZn_y$  phases and  
12 the surrounding Zn-rich interdendritic regions seem to remain intact. This suggests that micro-  
13 galvanic corrosion occurs between the components of the eutectic phase and between the  $\alpha$ -  
14 Mg dendrites and the interdendritic area (second phase + Zn-rich interdendritic region). It is  
15 worth mentioning that, due to the degradation, many small particles are visible along the  
16 boundaries between the  $\alpha$ -Mg dendrites and the interdendritic regions. The EDS analysis  
17 (Table 4) demonstrated that those particles are considerably rich in Zn, which is even higher  
18 than the original Zn-rich interdendritic regions (shown in Table 2).

19 In the case of extruded  $Mg_4Zn_{0.2}Sn$  alloy (Figs. 6c and 6d), the brighter Zn-rich matrix seems  
20 to be less corroded than the darker matrix. Moreover, a dark circle is formed around the Fe-  
21 Mn/ $Mg_2Si$  particle, revealing the occurrence of micro-galvanic corrosion between the impurity  
22 containing particle and the surrounding matrix. In comparison, much milder micro-galvanic  
23 corrosion can be noticed between the nearby  $Mg_xZn_y$  phases and the matrix (Fig. 6d), indicating  
24 the weaker galvanic effect. Some small holes are observed on the corroded surface (Fig. 6c),

1 which may be explained by the detachment of those impurity particles or tiny second phases  
2 as a result of undermining caused by the galvanic attack.

### 3 3.2.3 Surface and cross-sectional analysis after long-term immersion

4 Fig. 7 shows the surface and cross section morphologies of as-cast and extruded Mg<sub>4</sub>Zn<sub>0.2</sub>Sn  
5 alloys after exposure to 0.5 wt.% NaCl solution for 48 h. Apparently, localized corrosion occurs  
6 for both alloys but is more severe for the as-cast alloy. To be specific, for the as-cast alloy, the  
7 layer of corrosion products (Fig. 7a) formed on the surface is less compact. More and much  
8 deeper corrosion cavities can be observed in the cross-sectional morphology (Fig. 7b). Besides,  
9 some detached second phases (denoted by blue arrows in Fig. 7b) remain in the corrosion  
10 product layer. The partially protruded second phases in the corrosion product layer indicate  
11 that the surrounding Zn-rich interdendritic regions also dissolve to some extent. Moreover,  
12 small particles are noticed at the Zn-rich interdendritic region/corrosion product layer interface.  
13 The immersion test results of the as-cast Mg<sub>4</sub>Zn<sub>0.2</sub>Sn alloy agree well with the SKPFM and  
14 short immersion tests. The least noble  $\alpha$ -Mg matrix dissolves first, followed by the Zn-rich  
15 interdendritic regions, while the more noble Mg<sub>x</sub>Zn<sub>y</sub> phases serve as micro-cathodes during  
16 immersion. For the extruded Mg<sub>4</sub>Zn<sub>0.2</sub>Sn alloy, generally, shallow corrosion cavities appear  
17 at those dark matrix regions (denoted by yellow arrows in Fig. 7d), while the brighter matrixes  
18 (denoted by red arrows in Fig. 7d) remain as stilts. Small particles (denoted by blue arrows in  
19 Fig. 7d) are embedded in the corrosion product layer or aggregate at the interface of the bulk  
20 alloy and the corrosion products.

21 Element mappings (Fig. 8) were performed for the cross sections (the same positions shown in  
22 the inserted images in Figs. 7b and 7d) of both alloys to investigate the element distribution at  
23 the corroded interfaces. As expected, the corrosion product layers formed on the surfaces of  
24 both alloys are rich in oxygen (O). For the as-cast Mg<sub>4</sub>Zn<sub>0.2</sub>Sn alloy, it is revealed that the  $\alpha$ -  
25 Mg matrix dissolves preferentially, while the second phases together with the Zn-rich

1 interdendritic regions serve as a kind of barrier for the interior  $\alpha$ -Mg matrix. Moreover, those  
2 small particles located at the corroded interface are rich in Zn. They should be similar to the  
3 small particles (distributed along the boundaries of the  $\alpha$ -Mg matrix and the interdendritic  
4 regions) observed after short immersion tests (Figs. 6a and 6b). For the extruded alloy, the  
5 small particles in the corrosion product layers or at the alloy/corrosion product interfaces are  
6 also rich in Zn, which may be the remaining tiny second phases after corrosion. In addition,  
7 enrichment of Zn is noticed at the interface of the bulk material and the corrosion products  
8 layer, while the distribution of Sn is quite homogeneous. No  $Mg_2Si$  phases or Fe-Mn/ $Mg_2Si$   
9 particles were detected in the selected region for analysis probably because of the low content  
10 of them in the alloy (Fe, Si and Mn mapping results are not shown here).

#### 11 3.2.4 Potentiodynamic polarization curves

12 To compare the corrosion resistance of as-cast and extruded  $Mg_4Zn_{0.2}Sn$  alloys,  
13 potentiodynamic polarization curves were recorded after conditioning at OCP for different time  
14 intervals (see Fig. 9). When the conditioning time is 30 min, the polarization curves are quite  
15 noisy for both alloys, which may be a result of the active surface evolution during immersion.  
16 The corrosion potential ( $E_{corr}$ ) is slightly more positive after hot extrusion due to the higher  
17 cathodic current density. With extended conditioning time, both the cathodic and anodic  
18 current densities of the extruded alloy are lower than those of the as-cast alloy. Meanwhile, in  
19 all cases, the anodic current density increases rapidly with increasing potential and no retarded  
20 dissolution, e.g. by protective film formation, is observed in the anodic parts, which is typical  
21 for most of the Mg alloys [32-34]. This indicates that the corrosion product layers formed on  
22 both alloy surfaces are not protective enough to the anodic dissolution of the alloys.  
23 According to the measured and calculated parameters listed in Table 5, as-cast  $Mg_4Zn_{0.2}Sn$   
24 alloy possesses higher corrosion resistance than the extruded one when the OCP conditioning

1 time is 30 min. However, after 48 h, the extruded alloy shows a lower corrosion rate in 0.5 wt.%  
2 NaCl solution at room temperature.

### 3 3.2.5 Hydrogen evolution and weight loss

4 Hydrogen evolution and weight loss tests were also carried out to assess the integral corrosion  
5 rates of as-cast and extruded Mg<sub>4</sub>Zn<sub>0.2</sub>Sn alloys after exposure to 0.5 wt.% NaCl solution for  
6 up to 168 h at room temperature. According to the hydrogen evolution curves in Fig. 10a,  
7 generally, the as-cast Mg<sub>4</sub>Zn<sub>0.2</sub>Sn alloy evolves much more hydrogen than the extruded one  
8 during immersion. Moreover, the hydrogen evolution of the as-cast alloy follows an  
9 exponential growth, while it is a logarithmic growth (a slower increase at longer time) for the  
10 extruded alloy, indicating a much faster hydrogen evolution of as-cast alloy. As a result, the  
11 gap between the evolved volumes of hydrogen from the Mg<sub>4</sub>Zn<sub>0.2</sub>Sn alloy in the two different  
12 processing conditions becomes wider with extension of immersion time. The corrosion rates  
13 calculated according to the total volume of evolved hydrogen agree well with those determined  
14 by the weight loss, revealing that the long-term corrosion rate of Mg<sub>4</sub>Zn<sub>0.2</sub>Sn alloy is  
15 significantly reduced after hot extrusion.

## 16 4. Discussion

17 The solid solubility of Zn and Sn in Mg matrix is similar, dropping rapidly when the  
18 temperature is decreased from the eutectic temperature. For the Mg-Zn binary system, the  
19 solubility of Zn decreases from 6.2 wt.% at 325 °C to 1.6 wt.% at 25 °C [23, 35]. While in the  
20 Mg-Sn binary system, the equilibrium solid solubility of Sn declines substantially from 14.85  
21 wt.% at 561 °C to only 0.17 wt.% at room temperature [36, 37] Supersaturation of solute atoms  
22 in  $\alpha$ -Mg can still occur during casting due to the non-equilibrium solidification process [11].  
23 For the Mg-Zn-Sn ternary system, no ternary phases have been reported or confirmed neither  
24 by experimental nor by thermodynamic calculation [38-40]. However, a small amount of Zn  
25 can dissolve in the Mg<sub>2</sub>Sn binary phase [11, 41] and Sn can dissolve in the MgZn<sub>2</sub> phase [41,

1 42] but not in  $Mg_4Zn_7$  or  $MgZn$  precipitates according to the work of Sirkin et al. [43] and  
2 Mingolo et al. [38]. Therefore, the microstructure of the as-cast  $Mg_4Zn_{0.2}Sn$  alloy is composed  
3 of  $\alpha$ -Mg, Zn-supersaturated region and divorced eutectic phase ( $\alpha$ -Mg matrix +  $Mg_xZn_y$  phase)  
4 (Figs. 3a and 3b). After homogenization treatment and hot extrusion, most of the  $Mg_xZn_y$   
5 phases in the as-cast alloy are dissolved into the matrix as verified by the significantly  
6 decreased volume fraction of second phases (Fig. 3a), leading to the exposure of some Fe-  
7 Mn/ $Mg_2Si$  particles in the matrix. A small amount of tiny Mg-Zn binary phases dynamically  
8 precipitate on the grain boundaries and those Fe-Mn/ $Mg_2Si$  and single  $Mg_2Si$  particles are  
9 redistributed in the microstructure (Figs. 3c-3f). This is associated with the homogenization  
10 treatment which was applied prior to extrusion. Furthermore, it occurs concurrently due to the  
11 microstructure changes during the forming process, which includes the reformation of the  
12 microstructure due to dynamic recrystallization and also dynamic precipitation [1]. Thus, the  
13 coarse dendritic grains in the as-cast billets are substituted by fine recrystallized globular grains  
14 in the extruded alloy. Apart from the refinement of microstructure, redistribution of alloying  
15 elements is also concomitant with the extrusion process. Moreover, element segregation still  
16 exists, but only little attention has been paid in other reports regarding to the influence of  
17 distribution of segregated solute atoms on the corrosion behavior of wrought Mg alloys.

18 The corrosion process of  $Mg_4Zn_{0.2}Sn$  alloys in 0.5 wt.% NaCl solution is schematically  
19 illustrated in Fig. 11. In dry air, magnesium oxide (MgO) is instantaneously formed on Mg  
20 alloy surface at room temperature, which imparts good corrosion resistance to Mg alloys in  
21 such circumstance. In the presence of water, MgO reacts with it, generating magnesium  
22 hydroxide ( $Mg(OH)_2$ ). However, both MgO and  $Mg(OH)_2$  are water-soluble, resulting in the  
23 exposure of the underlying substrate to the solution [2, 44, 45]. Additionally, In the presence  
24 of  $Cl^-$ , local breakdown of the corrosion products layer can also occur, resulting in the exposure  
25 of the underneath substrate to the corrosive electrolyte and triggering localized corrosion. This

1 may be achieved by the formation of metal-hydroxyl-chloride complex compounds [46]. The  
2 highly negative electrode potential of Mg and the poor protection ability of the oxide/hydroxide  
3 surface film render Mg intrinsically prone to corrosion in aqueous environment. Moreover,  
4 when the nobler second phases, impurities and some other compounds, for example, noble  
5 inclusions, which can be locally polarized, are exposed due to the defective surface film,  
6 localized corrosion can be triggered [45]. As disclosed by the SKPFM study for as-cast  
7 Mg<sub>4</sub>Zn<sub>0.2</sub>Sn alloy (Fig. 5), the Mg<sub>x</sub>Zn<sub>y</sub> phases show higher Volta potential compared to the  
8 nearby  $\alpha$ -Mg matrix, which can form micro-galvanic couples with the matrix. Although the  
9 Volta potential map of the extruded alloy is lacked in this study, the short immersion tests (Figs.  
10 6c and 6d) and literature review [47, 48] demonstrate that the Fe-Mn/Mg<sub>2</sub>Si and single Mg<sub>2</sub>Si  
11 particles are nobler than  $\alpha$ -Mg matrix and may induce micro-galvanic corrosion. Therefore,  
12 localized corrosion was detected for both processing conditions according to the surface and  
13 cross-section morphologies after immersion (Figs. 6 and 7). The different relative Volta  
14 potential of each constituent influences the dissolution precedence during immersion, which is  
15 clearly revealed by observation of the cross section of the as-cast Mg<sub>4</sub>Zn<sub>0.2</sub>Sn alloy (Fig. 7b).  
16 Furthermore, the cross-section morphology of the extruded Mg<sub>4</sub>Zn<sub>0.2</sub>Sn alloy (Fig. 7d) reveals  
17 that galvanic effect also exists between the Zn segregated matrix and the normal  $\alpha$ -Mg matrix  
18 owing to the heterogeneous distribution of elements. After extrusion, fine second phases  
19 dynamically precipitate and either second phases or impurity particles are uniformly distributed  
20 in the alloy. Considering the low amount and the detachment of impurity particles after certain  
21 immersion time, the intensity of micro-galvanic coupling is reduced in the extruded  
22 Mg<sub>4</sub>Zn<sub>0.2</sub>Sn alloy compared to the as-cast one. More importantly, the presence of Mn favors  
23 the formation of Fe-Mn solid solution (Mn encapsulates Fe) instead of pure Fe particles as  
24 revealed in this study. Since the galvanic activity between Mn and Mg is less than that between  
25 Fe and Mg, the Fe-Mn particles would exhibit significantly lower electrocatalytic activity

1 towards hydrogen reduction reaction compared with pure Fe impurities [49-52]. Accordingly,  
2 the re-deposition process observed in the case of pure Fe impurities [53] can also be affected  
3 due to the altered self-corrosion behavior of Fe-Mn particles after detachment. The surrounding  
4 less active  $Mg_2Si$  phases may also contribute to that to some extent. Consequently, the  
5 corrosion rate of the alloy greatly decreases in spite of the micro-galvanic effect between the  
6 impurity particles and the  $\alpha$ -Mg matrix. Besides, the refined grain size of Mg alloys after  
7 extrusion has also been reported to enhance the corrosion resistance of Mg alloys, which is  
8 thought to be a result of the formation of more coherent surface layer on the refined  
9 microstructure [1, 54-56].

10 As revealed by the cross-section element mapping results (Fig. 8), Zn enriches at the surface  
11 film/substrate interface for both alloys, especially for the extruded one. Similar enrichment of  
12 alloying elements at the film/Mg alloy interfaces have been reported for Electron 717 alloy  
13 (Unocic et al.) [57, 58], AZ31 alloy (Cristóbal et al.) [59] and Mg5Sn3Zn alloy (Yang et al.)  
14 [60]. Moreover, according to the investigations carried out in refs. [58, 59, 61], it is speculated  
15 that the uniform enrichment of Zn at the entire film/alloy interface is related to the enhanced  
16 corrosion resistance of Mg alloys possibly by suppressing the outward migration of Mg.  
17 According to these literature, the segregation of Zn at the interface of Mg matrix and corrosion  
18 products is mainly attributed to two reasons. On the one hand, as corrosion proceeds in a  
19 relatively aggressive electrolyte, the active Mg atoms are selectively dissolved, leaving behind  
20 the inert Zn atoms [60]. Sn segregation can also occur for Mg5Sn3Zn alloy. However, given  
21 the much lower content of Sn in Mg4Zn0.2Sn alloy studied herein, only Zn segregation was  
22 detected at the surface film/substrate interface. On the other hand, in comparison with MgO,  
23 the lower thermodynamic stability of ZnO favors the enrichment of unreacted Zn at the  
24 corroding interface as corrosion proceeds [58]. Unocic et al. and Cristóbal et al. considered that  
25 the enriched Zn existed in metallic form based on EDS line profile (the peaks of O and Zn did

1 not correlate with each other) and XPS analysis. While Yang et al. identified the XPS region  
2 spectra of Zn 2p<sub>3/2</sub> to be the mixture of ZnO and metallic Zn, which might be ambiguous  
3 because of the strong overlap between the binding energy of Zn<sup>2+</sup> and Zn<sup>0</sup>. This was also  
4 mentioned by Cristóbal et al. and they determined the chemical state of Zn more effectively by  
5 measuring both FWHM value and the splitting value (2p<sub>1/2</sub>-2p<sub>3/2</sub>). The concentrated Zn behaves  
6 differently at the interfaces of the two alloys, i.e., existing as dispersed Zn-rich particles in the  
7 as-cast Mg<sub>4</sub>Zn<sub>0.2</sub>Sn alloy (Figs. 6a and 6b) while continuously distributed along the  
8 film/substrate interface in the extruded alloy (Fig. 8). This may be a result of the almost perfect  
9 solid solution state of the alloy reached after homogenization and extrusion.  
10 Therefore, it can be concluded that the extrusion process refines the microstructure (grain size  
11 and second phases) of Mg<sub>4</sub>Zn<sub>0.2</sub>Sn alloy, leads to more homogenous distribution of alloying  
12 elements (Zn and Sn) and impurities (Fe, Mn and Si), thereby resulting in a weakened micro-  
13 galvanic effect and an enhanced Zn segregation at the corrosion interface. Finally, this  
14 contribute to slightly denser corrosion products layer during immersion and weaker localized  
15 corrosion. The nobler second phases are the main driving force for the severe localized  
16 corrosion in the as-cast alloy, while mainly the Fe-Mn/Mg<sub>2</sub>Si particles are the cause for the  
17 extruded alloy.

## 18 **5. Conclusion**

19 In this study, the corrosion behavior of as-cast and extruded Mg<sub>4</sub>Zn<sub>0.2</sub>Sn alloys in 0.5 wt.%  
20 NaCl solution was compared. After extrusion, the microstructure of the as-cast alloy is greatly  
21 refined. The micron-sized eutectic phases ( $\alpha$ -Mg + Mg<sub>x</sub>Zn<sub>y</sub> phase) are replaced by tiny Mg-Zn  
22 precipitates and a few Fe-Mn/Mg<sub>2</sub>Si impurity particles. Interestingly, even after  
23 homogenization and extrusion, Zn segregated regions which are alternately distributed between  
24  $\alpha$ -Mg matrix still exists in the extruded alloy. Micro-galvanic couples are formed as expected  
25 from the Volta potential differences of those second phases, precipitates, Zn-rich areas and the

1  $\alpha$ -Mg matrix, resulting in localized corrosion behavior of both alloys. The localized corrosion  
2 is more severe for the as-cast alloy because of the large volume fraction of eutectic phases ( $\alpha$ -  
3 Mg matrix +  $Mg_xZn_y$  phase). However, hot extrusion significantly refines the microstructure  
4 of the alloy and homogenizes the distributions of alloying elements (Zn and Sn), which largely  
5 weakened the localized corrosion of extruded  $Mg_{40}Zn_{0.2}Sn$  alloy.

#### 6 **Declaration of interests**

7 The authors declare that there is no conflict of interests.

#### 8 **Data availability**

9 The raw/processed data required to reproduce these findings cannot be shared at this time as  
10 the data also forms part of an ongoing study.

#### 11 **Acknowledgement**

12 The author Pingli Jiang (CSC No. 201606310043) would like to thank the financial support  
13 from China Scholarship Council (CSC). The technical support from Mr. Ulrich Burmester and  
14 Mr. Volker Heitmann and the general discussion from our colleagues in the Division of  
15 Corrosion and Surface Technology department is gratefully acknowledged.

16

## 1 Reference

- 2 [1] Z.R. Zeng, N. Stanford, C.H.J. Davies, J.F. Nie, N. Birbilis, Magnesium extrusion alloys:  
3 a review of developments and prospects, *Int. Mater. Rev.*, 64 (2019) 27-62.  
4 <https://doi.org/10.1080/09506608.2017.1421439>.
- 5 [2] K. Gusieva, C.H.J. Davies, J.R. Scully, N. Birbilis, Corrosion of magnesium alloys: the role  
6 of alloying, *Int. Mater. Rev.*, 60 (2015) 169-194.  
7 <https://doi.org/10.1179/1743280414Y.0000000046>.
- 8 [3] T.B. Abbott, Magnesium: industrial and research developments over the last 15 years,  
9 *Corrosion*, 71 (2014) 120-127. <https://doi.org/10.5006/1474>.
- 10 [4] G.H. Zhang, J.H. Chen, H.G. Yan, B. Su, X. He, M. Ran, Effects of artificial aging on  
11 microstructure and mechanical properties of the Mg–4.5Zn–4.5Sn–2Al alloy, *J. Alloy. Compd.*,  
12 592 (2014) 250-257. <https://doi.org/10.1016/j.jallcom.2013.12.250>.
- 13 [5] H. Ibrahim, A.D. Klarner, B. Poorganji, D. Dean, A.A. Luo, M. Elahinia, Microstructural,  
14 mechanical and corrosion characteristics of heat-treated Mg-1.2Zn-0.5Ca (wt%) alloy for use  
15 as resorbable bone fixation material, *J. Mech. Behav. Biomed. Mater.*, 69 (2017) 203-212.  
16 <https://doi.org/10.1016/j.jmbbm.2017.01.005>.
- 17 [6] R.G. Guan, A.F. Cipriano, Z.Y. Zhao, J. Lock, D. Tie, T. Zhao, T. Cui, H.N. Liu,  
18 Development and evaluation of a magnesium–zinc–strontium alloy for biomedical  
19 applications—Alloy processing, microstructure, mechanical properties, and biodegradation,  
20 *Mater. Sci. Eng. C*, 33 (2013) 3661-3669. <https://doi.org/10.1016/j.msec.2013.04.054>.
- 21 [7] Q.M. Peng, X.J. Li, N. Ma, R.P. Liu, H.J. Zhang, Effects of backward extrusion on  
22 mechanical and degradation properties of Mg–Zn biomaterial, *J. Mech. Behav. Biomed. Mater.*,  
23 10 (2012) 128-137. <https://doi.org/10.1016/j.jmbbm.2012.02.024>.
- 24 [8] W.Q. Xu, N. Birbilis, G. Sha, Y. Wang, J.E. Daniels, Y. Xiao, M. Ferry, A high-specific-  
25 strength and corrosion-resistant magnesium alloy, *Nature Mater.*, 14 (2015) 1229-1235.  
26 <https://doi.org/10.1038/nmat4435>.
- 27 [9] P.L. Jiang, C. Blawert, R.Q. Hou, N. Scharnagl, J. Bohlen, M.L. Zheludkevich,  
28 Microstructural influence on corrosion behavior of MgZnGe alloy in NaCl solution, *J. Alloy.*  
29 *Compd.*, 783 (2019) 179-192. <https://doi.org/10.1016/j.jallcom.2018.12.296>.
- 30 [10] J.H. Chen, Z. Chen, H.G. Yan, F.Q. Zhang, K. Liao, Effects of Sn addition on  
31 microstructure and mechanical properties of Mg–Zn–Al alloys, *J. Alloy. Compd.*, 461 (2008)  
32 209-215. <https://doi.org/10.1016/j.jallcom.2007.07.066>.
- 33 [11] S.H. Wei, T.P. Zhu, M. Hodgson, W. Gao, Effects of Sn addition on the microstructure  
34 and mechanical properties of as-cast, rolled and annealed Mg–4Zn alloys, *Mater. Sci. Eng. A*,  
35 585 (2013) 139-148. <https://doi.org/10.1016/j.msea.2013.07.051>.
- 36 [12] Y.F. Chai, B. Jiang, J.F. Song, B. Liu, G.S. Huang, D.F. Zhang, F.S. Pan, Effects of Zn  
37 and Ca addition on microstructure and mechanical properties of as-extruded Mg-1.0 Sn alloy  
38 sheet, *Mater. Sci. Eng. A*, 746 (2019) 82-93. <https://doi.org/10.1016/j.msea.2019.01.028>.
- 39 [13] M. Esmaily, N. Mortazavi, M. Shahabi-Navid, J.E. Svensson, M. Halvarsson, L. Nyborg,  
40 M. Wessén, A.E.W. Jarfors, L.G. Johansson, Effect of rheocasting on corrosion of AM50 Mg  
41 alloy, *J. Electrochem. Soc.*, 162 (2015) C85-C95. DOI: 10.1149/2.0331503jes.
- 42 [14] S.H. Cai, T. Lei, N.F. Li, F.F. Feng, Effects of Zn on microstructure, mechanical properties  
43 and corrosion behavior of Mg–Zn alloys, *Mater. Sci. Eng. C*, 32 (2012) 2570-2577.  
44 <https://doi.org/10.1016/j.msec.2012.07.042>.

- 1 [15] E. Koç, M.B. Kannan, M. Ünal, E. Candan, Influence of zinc on the microstructure,  
2 mechanical properties and in vitro corrosion behavior of magnesium–zinc binary alloys, *J.*  
3 *Alloy. Compd.*, 648 (2015) 291-296. <https://doi.org/10.1016/j.jallcom.2015.06.227>.
- 4 [16] H.R. Bakhsheshi-Rad, E. Hamzah, A. Fereidouni-Lotfabadi, M. Daroonparvar, M.A.M.  
5 Yajid, M. Mezbahul-Islam, M. Kasiri-Asgarani, M. Medraj, Microstructure and bio-corrosion  
6 behavior of Mg–Zn and Mg–Zn–Ca alloys for biomedical applications, *Mater. Corros.*, 65  
7 (2014) 1178-1187. <https://doi.org/10.1002/maco.201307588>.
- 8 [17] B.P. Zhang, Y. Wang, L. Geng, Research on Mg–Zn–Ca alloy as degradable biomaterial,  
9 in: Rosario Pignatello, *Biomaterials-Physics and Chemistry*, InTech, Croatia, 2011, pp. 183-  
10 204.
- 11 [18] W.Y. Jiang, J.F. Wang, Q.S. Liu, W.K. Zhao, D.M. Jiang, S.F. Guo, Low hydrogen release  
12 behavior and antibacterial property of Mg-4Zn-xSn alloys, *Mater. Lett.*, 241 (2019) 88-91.  
13 <https://doi.org/10.1016/j.matlet.2019.01.048>.
- 14 [19] C.Y. Zhao, F.S. Pan, S. Zhao, H.C. Pan, K. Song, A.T. Tang, Preparation and  
15 characterization of as-extruded Mg–Sn alloys for orthopedic applications, *Mater. Des.*, 70  
16 (2015) 60-67. <https://doi.org/10.1016/j.matdes.2014.12.041>.
- 17 [20] W.Y. Jiang, J.F. Wang, W.K. Zhao, Q.S. Liu, D.M. Jiang, S.F. Guo, Effect of Sn addition  
18 on the mechanical properties and bio-corrosion behavior of cytocompatible Mg–4Zn based  
19 alloys, *J. Magnes. Alloy.*, 7 (2019) 15-26. <https://doi.org/10.1016/j.jma.2019.02.002>.
- 20 [21] A.A. Luo, A. Sachdev, Applications of magnesium alloys in automotive engineering, in:  
21 *Advances in wrought magnesium alloys: Fundamentals of processing, properties and*  
22 *applications*, C. Bettles, M. Barnett (Eds.), Woodhead Publishing Limited, Cambridge, 2012,  
23 pp. 393-426.
- 24 [22] R.H. Buzolin, M. Mohedano, C.L. Mendis, B. Mingo, D. Tolnai, C. Blawert, K.U. Kainer,  
25 H. Pinto, N. Hort, As cast microstructures on the mechanical and corrosion behaviour of ZK40  
26 modified with Gd and Nd additions, *Mater. Sci. Eng. A*, 682 (2017) 238-247.  
27 <https://doi.org/10.1016/j.msea.2016.11.022>.
- 28 [23] S.X. Zhang, X.N. Zhang, C.L. Zhao, J.N. Li, Y. Song, C.Y. Xie, H. R. Tao, Y. Zhang,  
29 Y.H. He, Y. Jiang, Y.J. Bian, Research on an Mg–Zn alloy as a degradable biomaterial, *Acta*  
30 *biomater.*, 6 (2010) 626-640. <https://doi.org/10.1016/j.actbio.2009.06.028>.
- 31 [24] X.B. Liu, D.Y. Shan, Y.W. Song, E.H. Han, Effects of heat treatment on corrosion  
32 behaviors of Mg-3Zn magnesium alloy, *T. Nonferr. Metal. Soc.*, 20 (2010) 1345-1350.  
33 [https://doi.org/10.1016/S1003-6326\(09\)60302-2](https://doi.org/10.1016/S1003-6326(09)60302-2).
- 34 [25] S. De Negri, M. Skrobańska, S. Delfino, A. Saccone, The Mg–Zn–Si system:  
35 Constitutional properties and phase formation during mechanical alloying, *Intermetallics*, 18  
36 (2010) 1722-1728. <https://doi.org/10.1016/j.intermet.2010.05.009>.
- 37 [26] E.L. Zhang, X.S. Wei, L. Yang, J.W. Xu, C.M. Song, Effect of Zn on the microstructure  
38 and mechanical properties of Mg–Si alloy, *Mater. Sci. Eng. A*, 527 (2010) 3195-3199.  
39 <https://doi.org/10.1016/j.msea.2010.01.074>.
- 40 [27] A. Kozlov, J. Gröbner, R. Schmid-Fetzer, Phase formation in Mg–Sn–Si and Mg–Sn–Si–  
41 Ca alloys, *J. Alloy Compd.*, 509 (2011) 3326-3337.  
42 <https://doi.org/10.1016/j.jallcom.2010.12.052>.
- 43 [28] A. Atrens, M. Liu, N.I.Z. Abidin, Corrosion mechanism applicable to biodegradable  
44 magnesium implants, *Mater. Sci. Eng. B*, 176 (2011) 1609-1636.  
45 <https://doi.org/10.1016/j.mseb.2010.12.017>.

- 1 [29] S. Pawar, X. Zhou, G.E. Thompson, G. Scamans, Z. Fan, The role of intermetallics on the  
2 corrosion initiation of twin roll cast AZ31 Mg alloy, *J. Electrochem. Soc.*, 162 (2015) C442-  
3 C448. DOI: 10.1149/2.0291509jes.
- 4 [30] R. Takei, H. Imai, J. Umeda, K. Kondoh, Relationship between surface potential  
5 difference and galvanic corrosion of magnesium alloy using SKPFM, *Transactions of JWRI*,  
6 39 (2010) 75-80.
- 7 [31] K.A. Yasakau, D. Höche, S.L. Lamaka, M.G.S. Ferreira, M.L. Zheludkevich, Kelvin  
8 microprobe analytics on iron-enriched corroded magnesium surface, *Corrosion*, 73 (2017) 583-  
9 595. <https://doi.org/10.5006/2260>.
- 10 [32] G.L. Song, A.L. Bowles, D.H. StJohn, Corrosion resistance of aged die cast magnesium  
11 alloy AZ91D, *Mater. Sci. Eng. A*, 366 (2004) 74-86.  
12 <https://doi.org/10.1016/j.msea.2003.08.060>.
- 13 [33] G. Song, S.Z. Song, A possible biodegradable magnesium implant material, *Adv. Eng.*  
14 *Mater.*, 9 (2007) 298-302. <https://doi.org/10.1002/adem.200600252>.
- 15 [34] G. Song, Recent progress in corrosion and protection of magnesium alloys, *Adv. Eng.*  
16 *Mater.*, 7 (2005) 563-586. <https://doi.org/10.1002/adem.200500013>.
- 17 [35] H. Okamoto, Comment on Mg-Zn (magnesium-zinc), *J. Phase Equilib.*, 15 (1994) 129-  
18 130.
- 19 [36] H. Liu, Y. Chen, Y. Tang, S. Wei, G. Niu, The microstructure, tensile properties, and creep  
20 behavior of as-cast Mg-(1-10)% Sn alloys, *J. Alloy. Compd.*, 440 (2007) 122-126.  
21 <https://doi.org/10.1016/j.jallcom.2006.09.024>.
- 22 [37] F.R. Elsayed, T.T. Sasaki, C.L. Mendis, T. Ohkubo, K. Hono, Compositional optimization  
23 of Mg-Sn-Al alloys for higher age hardening response, *Mater. Sci. Eng. A*, 566 (2013) 22-29.  
24 <https://doi.org/10.1016/j.msea.2012.12.041>.
- 25 [38] N. Mingolo, E. Nassif, B. Arcondo, H. Sirkin, Two competitive effects in the glass-  
26 forming ability of Mg-based alloys, *J. Non-cryst. Solids*, 113 (1989) 161-166.  
27 [https://doi.org/10.1016/0022-3093\(89\)90006-9](https://doi.org/10.1016/0022-3093(89)90006-9).
- 28 [39] C.L. Mendis, C.J. Bettles, M.A. Gibson, C.R. Hutchinson, An enhanced age hardening  
29 response in Mg-Sn based alloys containing Zn, *Mater. Sci. Eng. A*, 435 (2006) 163-171.  
30 <https://doi.org/10.1016/j.msea.2006.07.090>.
- 31 [40] F.G. Meng, J. Wang, L.B. Liu, Z.P. Jin, Thermodynamic modeling of the Mg-Sn-Zn  
32 ternary system, *J. Alloy. Compd.*, 508 (2010) 570-581.  
33 <https://doi.org/10.1016/j.jallcom.2010.08.124>.
- 34 [41] T. Godecke, F. Sommer, Stable and metastable phase equilibria in MgZn<sub>2</sub>-Zn and Mg<sub>2</sub>Sn-  
35 MgZn<sub>2</sub>-Sn-Zn alloys, *Z. Metallkd.*, 85 (1994) 683-691.
- 36 [42] E.I. Gladyshevskii, E.E. Cherkashin, Solid solutions on the basis of metallic compounds,  
37 *J. Inorg. Chem.-USSR*, 1 (1956) 288-295.
- 38 [43] H. Sirkin, N. Mingolo, E. Nassif, B. Arcondo, Increase of the glass-forming composition  
39 range of Mg-based binary alloys by addition of tin, *J. Non-cryst. Solids*, 93 (1987) 323-330.  
40 [https://doi.org/10.1016/S0022-3093\(87\)80178-3](https://doi.org/10.1016/S0022-3093(87)80178-3).

- 1 [44] G.L. Song, A. Atrens, Understanding magnesium corrosion—a framework for improved  
2 alloy performance, *Adv. Eng. Mater.*, 5 (2003) 837-858.  
3 <https://doi.org/10.1002/adem.200310405>.
- 4 [45] M. Esmaily, J.E. Svensson, S. Fajardo, N. Birbilis, G.S. Frankel, S. Virtanen, R. Arrabal,  
5 S. Thomas, L.G. Johansson, Fundamentals and advances in magnesium alloy corrosion, *Prog.*  
6 *Mater. Sci.*, 89 (2017) 92-193. <https://doi.org/10.1016/j.pmatsci.2017.04.011>.
- 7 [46] L. Wang, B.P. Zhang, T. Shinohara, Corrosion behavior of AZ91 magnesium alloy in  
8 dilute NaCl solutions, *Mater. Des.*, 31 (2010) 857-863.  
9 <https://doi.org/10.1016/j.matdes.2009.07.049>.
- 10 [47] F. Andreatta, I. Apachitei, A.A. Kodentsov, J. Dzwonczyk, J. Duszczyk, Volta potential  
11 of second phase particles in extruded AZ80 magnesium alloy, *Electrochim. Acta*, 51 (2006)  
12 3551-3557. <https://doi.org/10.1016/j.electacta.2005.10.010>.
- 13 [48] G. Ben-Hamu, D. Eliezer, K.S. Shin, The role of Si and Ca on new wrought Mg–Zn–Mn  
14 based alloy, *Mater. Sci. Eng. A*, 447 (2007) 35-43. <https://doi.org/10.1016/j.msea.2006.10.059>.
- 15 [49] G.L. Song, A. Atrens, Corrosion mechanisms of magnesium alloys, *Adv. Eng. Mater.*, 1  
16 (1999) 11-33. [https://doi.org/10.1002/\(SICI\)1527-2648\(199909\)1:1%3C11::AID-  
17 ADEM11%3E3.0.CO;2-N](https://doi.org/10.1002/(SICI)1527-2648(199909)1:1%3C11::AID-ADEM11%3E3.0.CO;2-N).
- 18 [50] H.A. Robinson, P.F. George, Effect of alloying and impurity elements in magnesium alloy  
19 cast anodes, *Corrosion*, 10 (1954) 182-188. <https://doi.org/10.5006/0010-9312-10.6.182>.
- 20 [51] H. Matsubara, Y. Ichige, K. Fujita, H. Nishiyama, K. Hodouchi, Effect of impurity Fe on  
21 corrosion behavior of AM50 and AM60 magnesium alloys, *Corros. Sci.*, 66 (2013) 203-210.  
22 <https://doi.org/10.1016/j.corsci.2012.09.021>.
- 23 [52] D.S. Gandel, M.A. Easton, M.A. Gibson, N. Birbilis, CALPHAD simulation of the Mg–  
24 (Mn, Zr)–Fe system and experimental comparison with as-cast alloy microstructures as  
25 relevant to impurity driven corrosion of Mg-alloys, *Mater. Chem. and Phys.*, 143 (2014) 1082-  
26 1091. <https://doi.org/10.1016/j.matchemphys.2013.11.008>.
- 27 [53] D. Höche, S.V. Lamaka, B. Vaghefinazari, T. Braun, R.P. Petruskas, M. Fichtner, M.L.  
28 Zheludkevich, Performance boost for primary magnesium cells using iron complexing agents  
29 as electrolyte additives, *Sci. Rep.-UK*, 8 (2018) 7578. DOI:10.1038/s41598-018-25789-8.
- 30 [54] Y.L. Zhou, Y.C. Li, D.M. Luo, Y.F. Ding, P. Hodgson, Microstructures, mechanical and  
31 corrosion properties and biocompatibility of as extruded Mg–Mn–Zn–Nd alloys for biomedical  
32 applications, *Mater. Sci. Eng. C*, 49 (2015) 93-100. <https://doi.org/10.1016/j.msec.2014.12.057>.
- 33 [55] G.R. Argade, S.K. Panigrahi, R.S. Mishra, Effects of grain size on the corrosion resistance  
34 of wrought magnesium alloys containing neodymium, *Corros. Sci.*, 58 (2012) 145-151.  
35 <https://doi.org/10.1016/j.corsci.2012.01.021>.
- 36 [56] N.N. Aung, W. Zhou, Effect of grain size and twins on corrosion behaviour of AZ31B  
37 magnesium alloy, *Corros. Sci.*, 52 (2010) 589-594.  
38 <https://doi.org/10.1016/j.corsci.2009.10.018s>.
- 39 [57] M.P. Brady, G. Rother, L.M. Anovitz, K.C. Littrell, K.A. Unocic, H.H. Elsentriecy, G. L.  
40 Song, J.K. Thomson, N.C. Gallego, B. Davis, Film breakdown and nano-porous Mg (OH)<sub>2</sub>  
41 formation from corrosion of magnesium alloys in salt solutions, *J. Electrochem. Soc.*, 162  
42 (2015) C140-C149. DOI: 10.1149/2.0171504jes.
- 43 [58] K.A. Unocic, H.H. Elsentriecy, M.P. Brady, H.M. Meyer, G.L. Song, M. Fayek, R.A.  
44 Meisner, B. Davis, Transmission electron microscopy study of aqueous film formation and

1 evolution on magnesium alloys, J. Electrochem. Soc., 161 (2014) C302-C311. DOI:  
2 10.1149/2.024406jes.  
3 [59] M.J. Cristóbal, D. Gesto, P. Minino, G. Pena, P. Rey, D. Verdera, An XPS analysis of the  
4 oxide surface layers formed on a friction stir processed magnesium alloy, Surf. Interface Anal.,  
5 44 (2012) 1030-1034. <https://doi.org/10.1002/sia.4859>.  
6 [60] J. Yang, C.D. Yim, B.S. You, Effects of solute Zn on corrosion film of Mg–Sn–Zn alloy  
7 formed in NaCl solution, J. Electrochem. Soc., 163 (2016) C839-C844. DOI:  
8 10.1149/2.0401614jes.  
9 [61] R.C. Phillips, J.R. Kish, Nature of surface film on matrix phase of Mg alloy AZ80 formed  
10 in water, Corrosion, 69 (2013) 813-820. <https://doi.org/10.5006/0938>.  
11

## 1 **Figure Captions**

2 **Fig. 1.** Phase diagram of Mg<sub>4</sub>Zn-Sn system calculated by Pandat.

3 **Fig. 2.** Microstructures of (a) as-cast and (b) extruded Mg<sub>4</sub>Zn<sub>0.2</sub>Sn alloys determined by  
4 optical microscope (ED: extrusion direction).

5 **Fig. 3.** Microstructures of (a, d) as-cast Mg<sub>4</sub>Zn<sub>0.2</sub>Sn alloy and (b, c, e, f) extruded  
6 Mg<sub>4</sub>Zn<sub>0.2</sub>Sn alloy along (b, e) extrusion direction and (c, f) transverse direction taken by SEM  
7 in BSE mode (ED: extrusion direction).

8 **Fig. 4.** Element distribution for the microstructure of as-cast and extruded (in transverse  
9 direction) Mg<sub>4</sub>Zn<sub>0.2</sub>Sn alloys determined by EDS mapping.

10 **Fig. 5.** (a) Topography, (b) surface Volta potential map and (c) a line-profile analysis of a  
11 second phase for as-cast Mg<sub>4</sub>Zn<sub>0.2</sub>Sn alloy studied by SKPFM.

12 **Fig. 6.** Surface morphologies of (a) as-cast and (b) extruded Mg<sub>4</sub>Zn<sub>0.2</sub>Sn alloys after  
13 immersion in 0.5 wt.% NaCl solution for 6 h at room temperature with removal of corrosion  
14 products. (c) and (d) are the enlarged details of the marked regions in (a) and (b) respectively.

15 **Fig. 7.** Surface and cross-sectional morphologies of (a, c) as-cast and (b, d) extruded  
16 Mg<sub>4</sub>Zn<sub>0.2</sub>Sn alloys after immersion in 0.5 wt.% NaCl solution at room temperature for 48 h  
17 (ED: extrusion direction).

18 **Fig. 8.** Element mappings for the cross sections of as-cast and extruded Mg<sub>4</sub>Zn<sub>0.2</sub>Sn alloys  
19 after immersed in 0.5 wt.% NaCl solution at room temperature for 48 h (ED: extrusion  
20 direction).

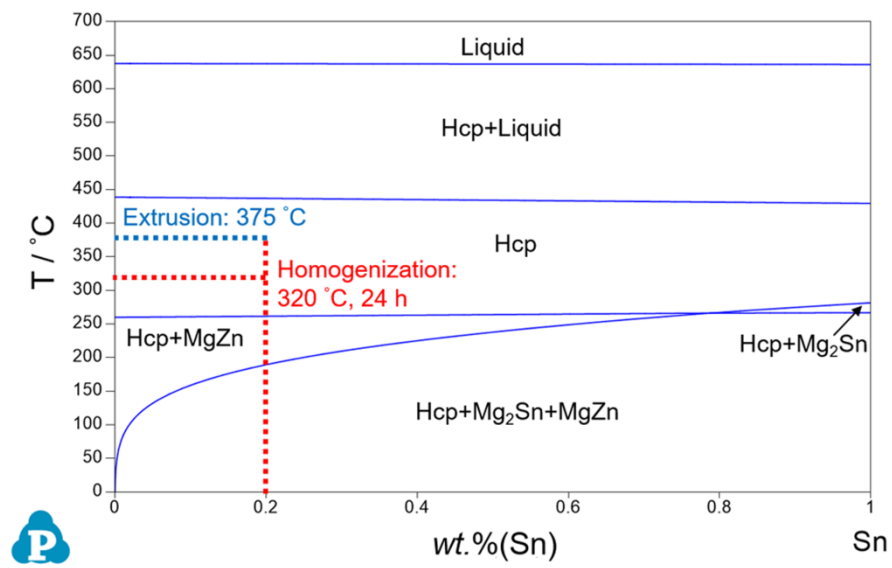
21 **Fig. 9.** Potentiodynamic polarization curves of as-cast and extruded Mg<sub>4</sub>Zn<sub>0.2</sub>Sn alloys after  
22 conditioned at OCP for different time at room temperature.

23 **Fig. 10.** (a) Hydrogen evolution curves and (b) corrosion rates calculated by evolved hydrogen  
24 volume and weight loss of as-cast and extruded Mg<sub>4</sub>Zn<sub>0.2</sub>Sn alloys after immersion in 0.5 wt.%  
25 NaCl solution for 168 h at room temperature.

26 **Fig. 11.** Schematic illustration for the corrosion process of as-cast and extruded Mg<sub>4</sub>Zn<sub>0.2</sub>Sn  
27 alloys in 0.5 wt.% NaCl solution.

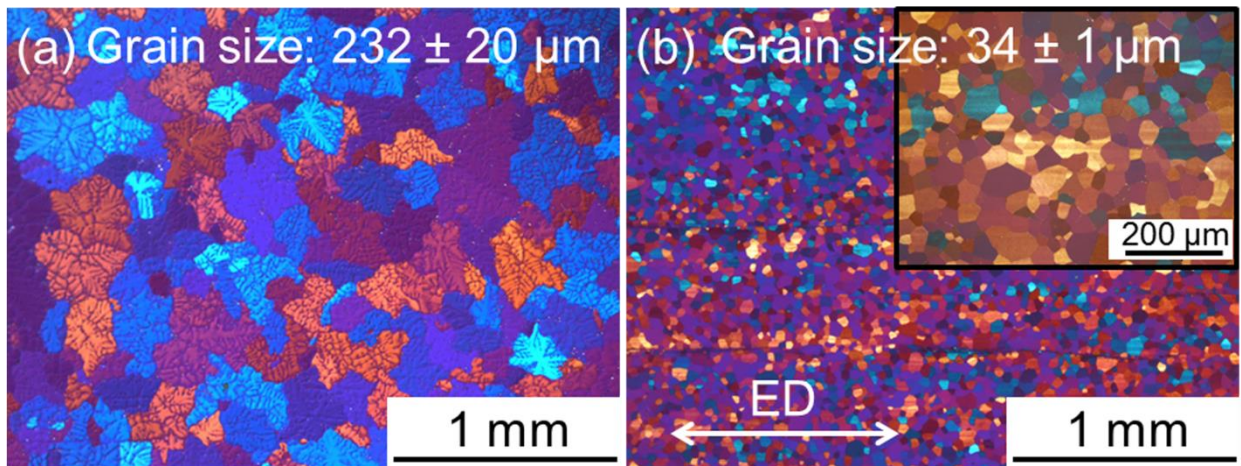
28

1 **Figure 1**



2

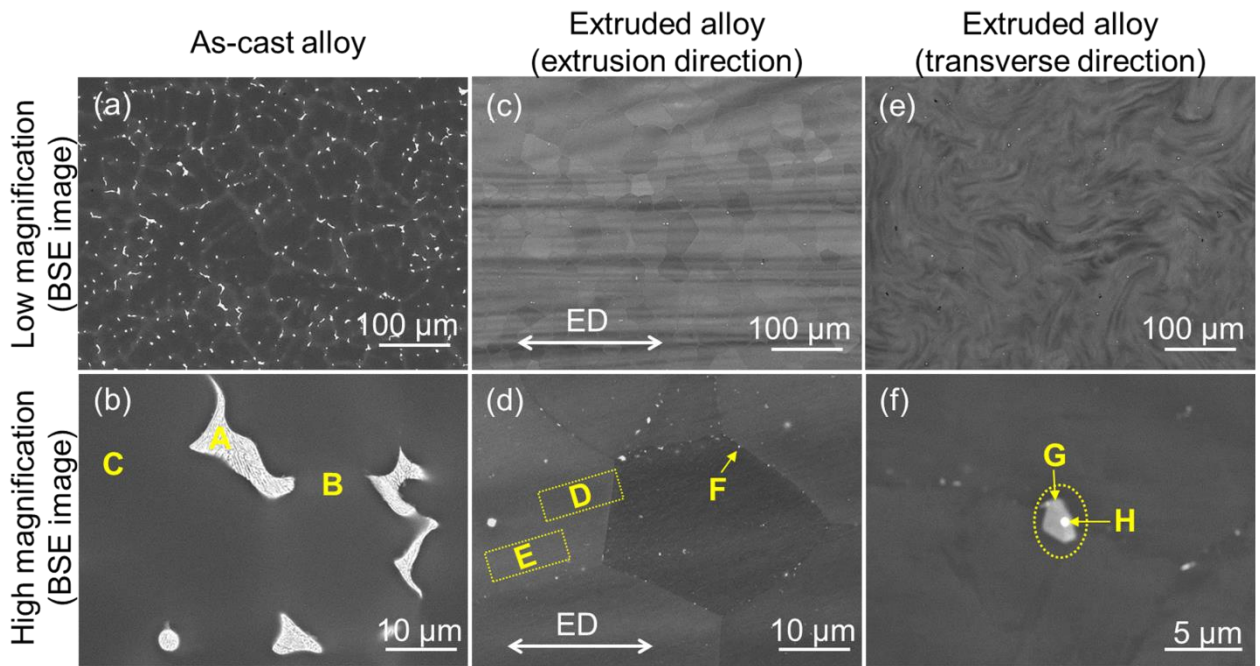
3 **Figure 2**



4

5

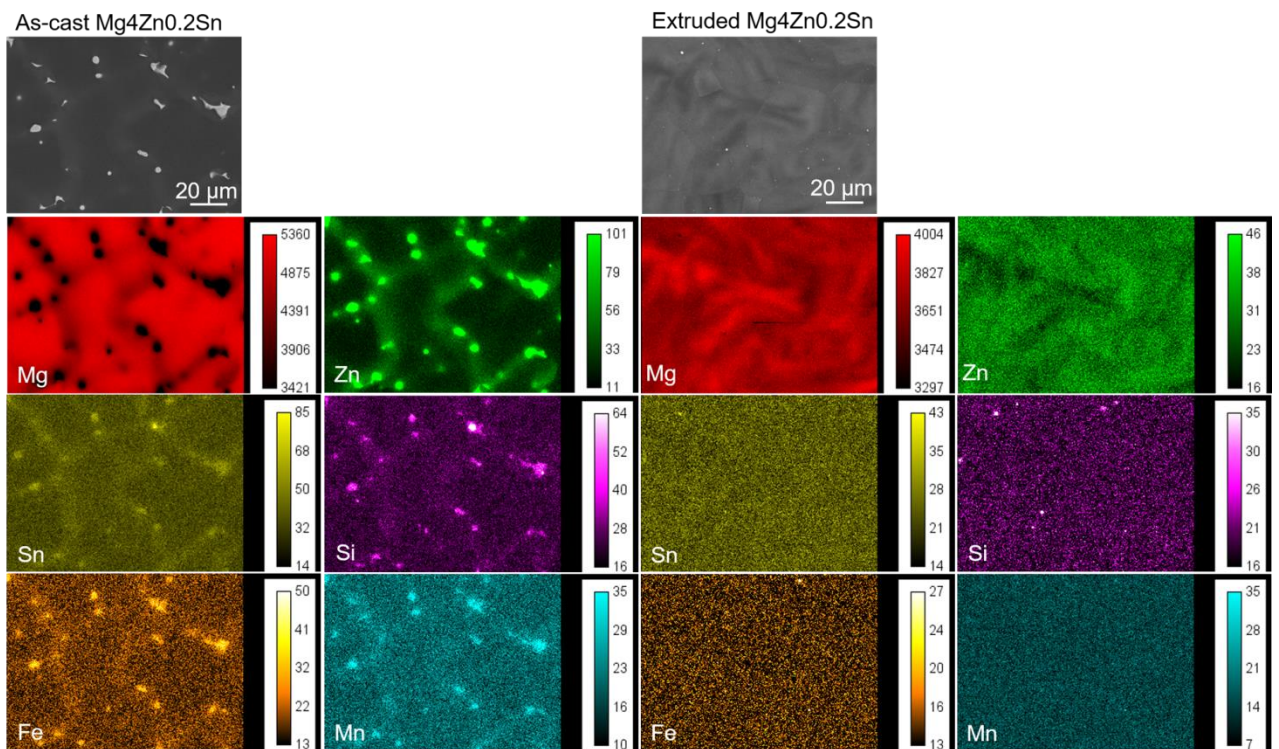
1 **Figure 3**



2

3

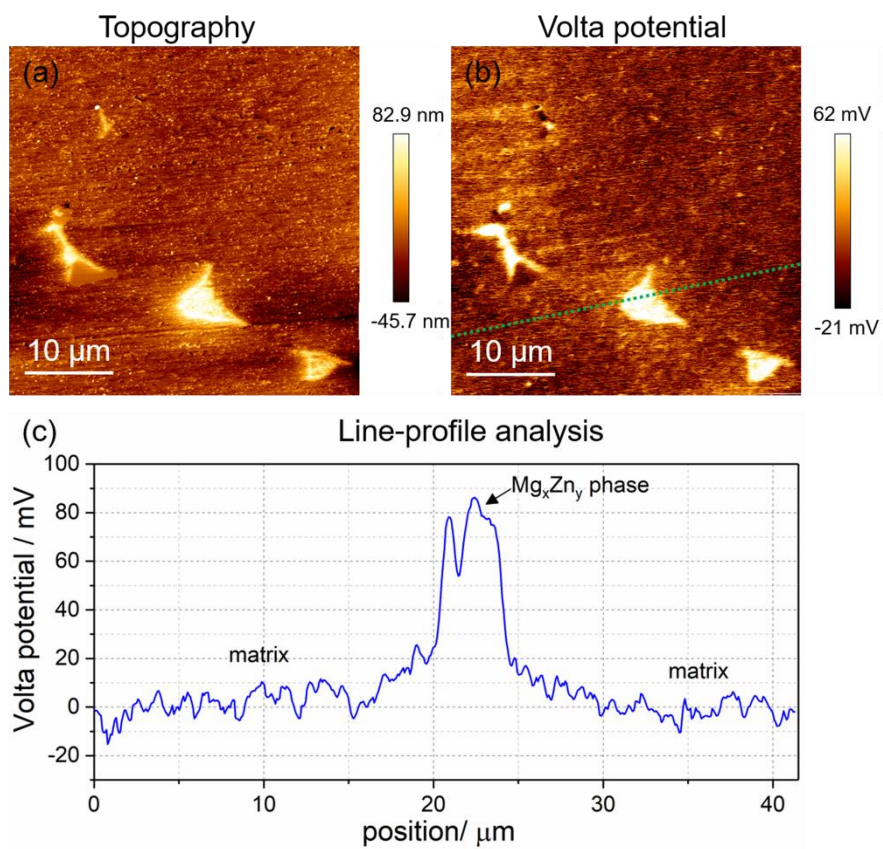
4 **Figure 4**



5

6

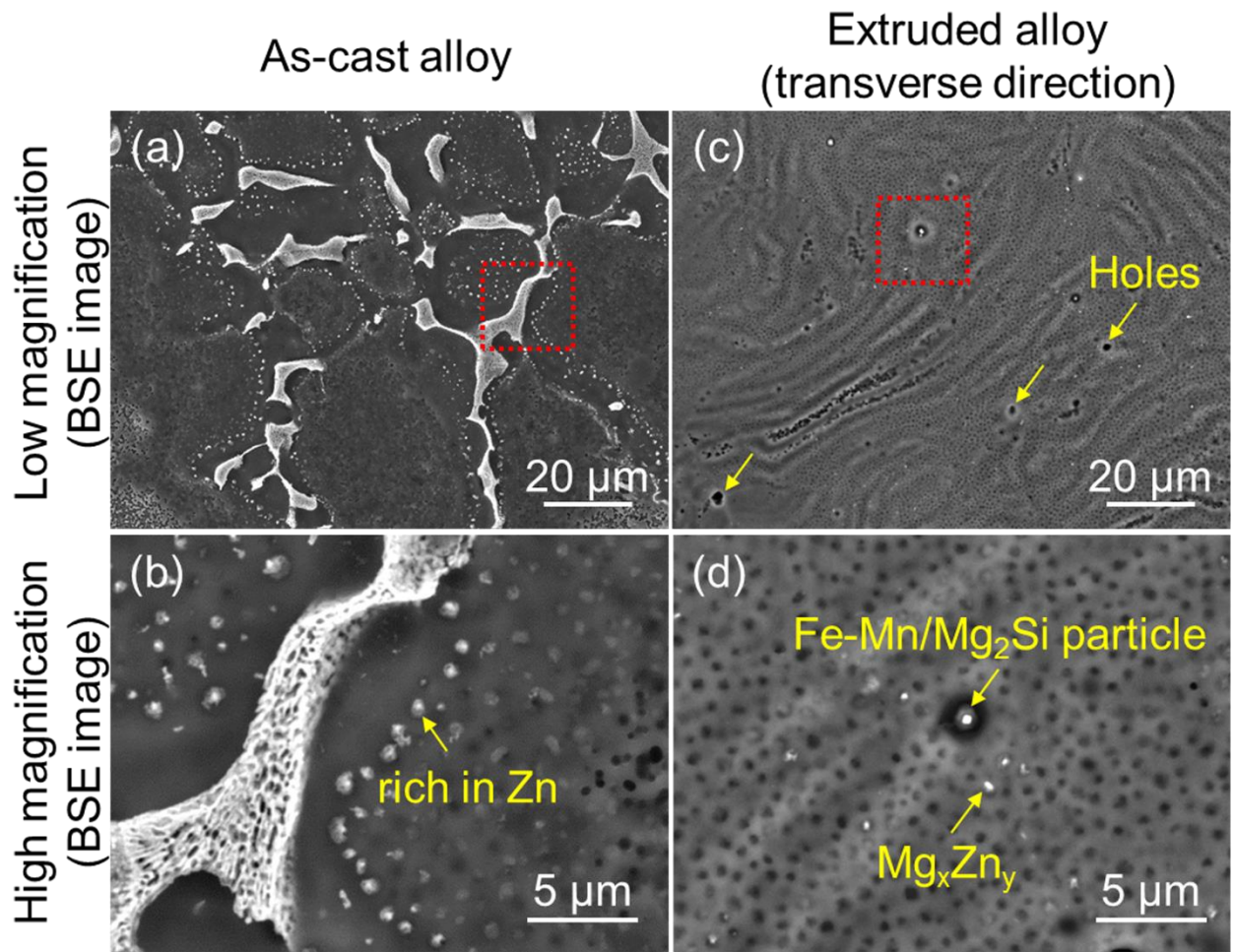
1 **Figure 5**



2

3

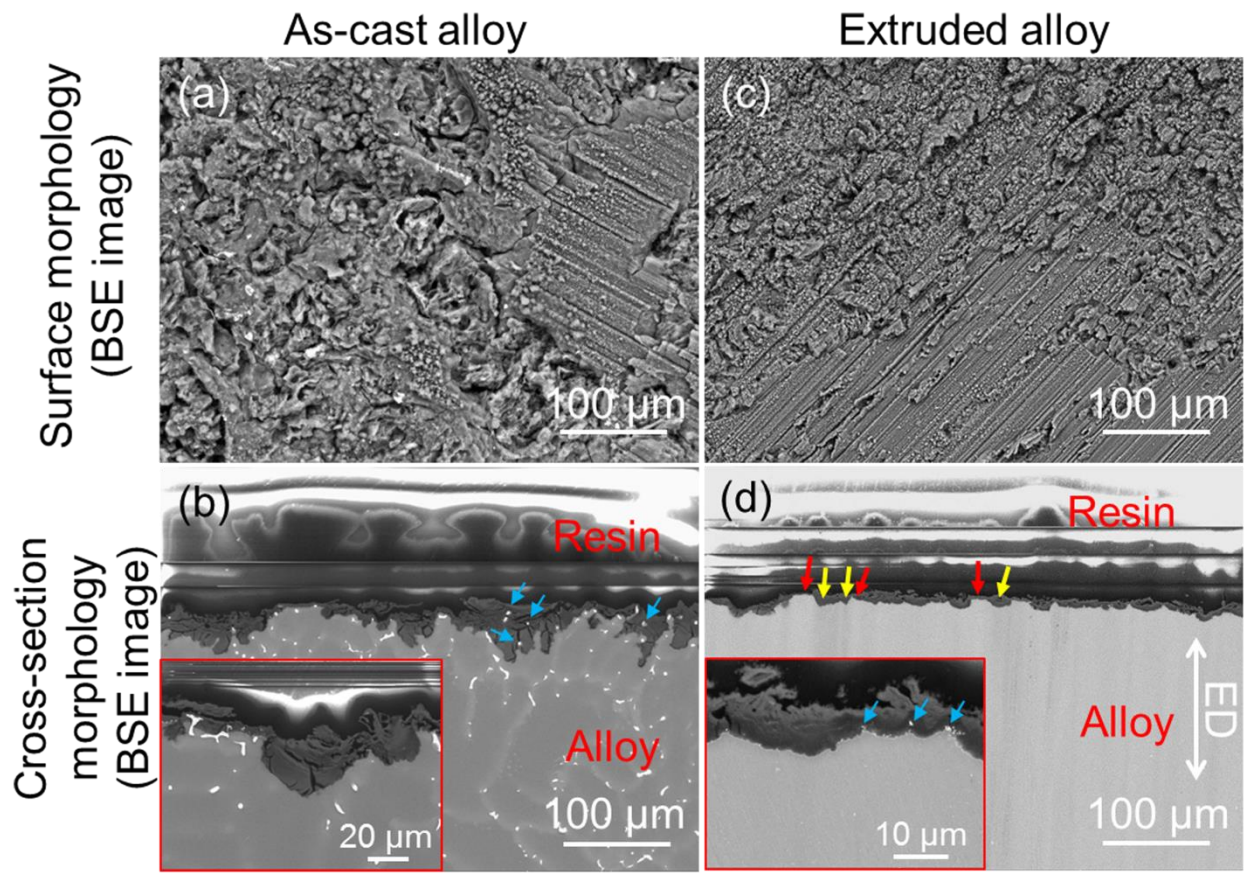
1 **Figure 6**



2

3

1 **Figure 7**

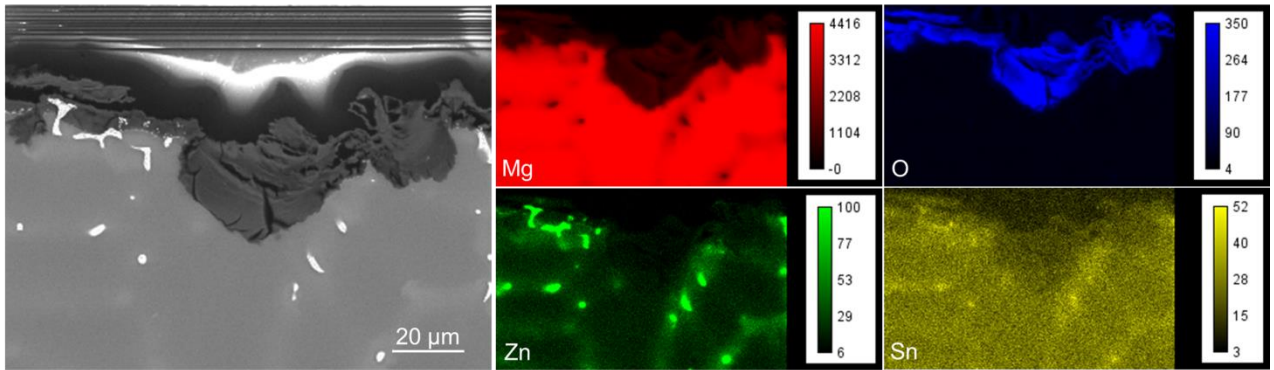


2

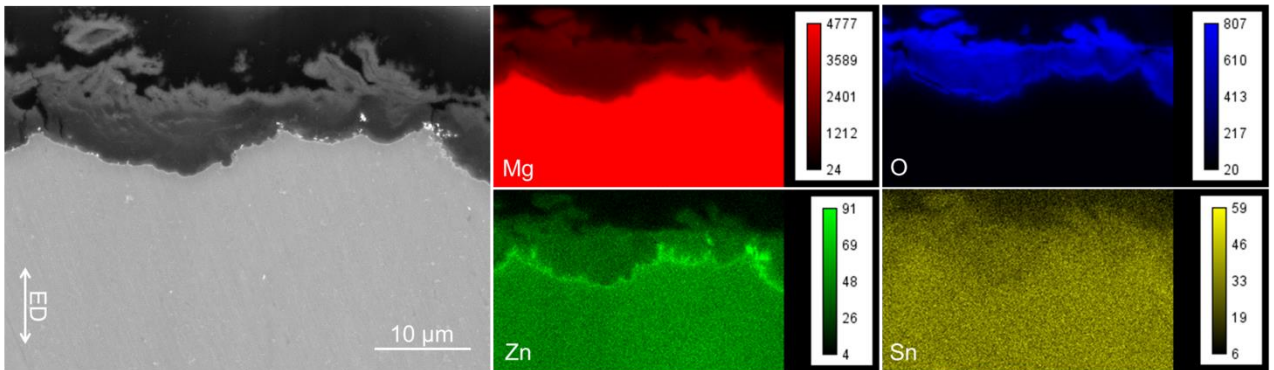
3

1 **Figure 8**

As-cast Mg<sub>4</sub>Zn<sub>0.2</sub>Sn

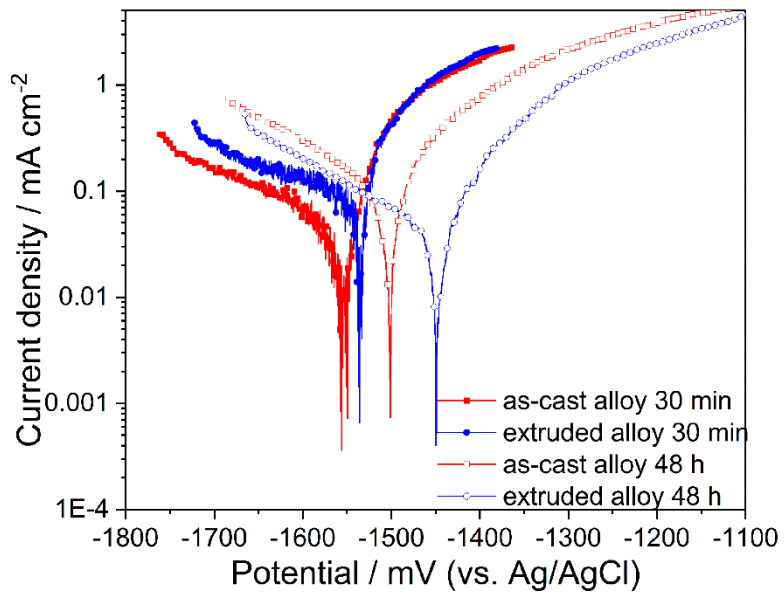


Extruded Mg<sub>4</sub>Zn<sub>0.2</sub>Sn



2

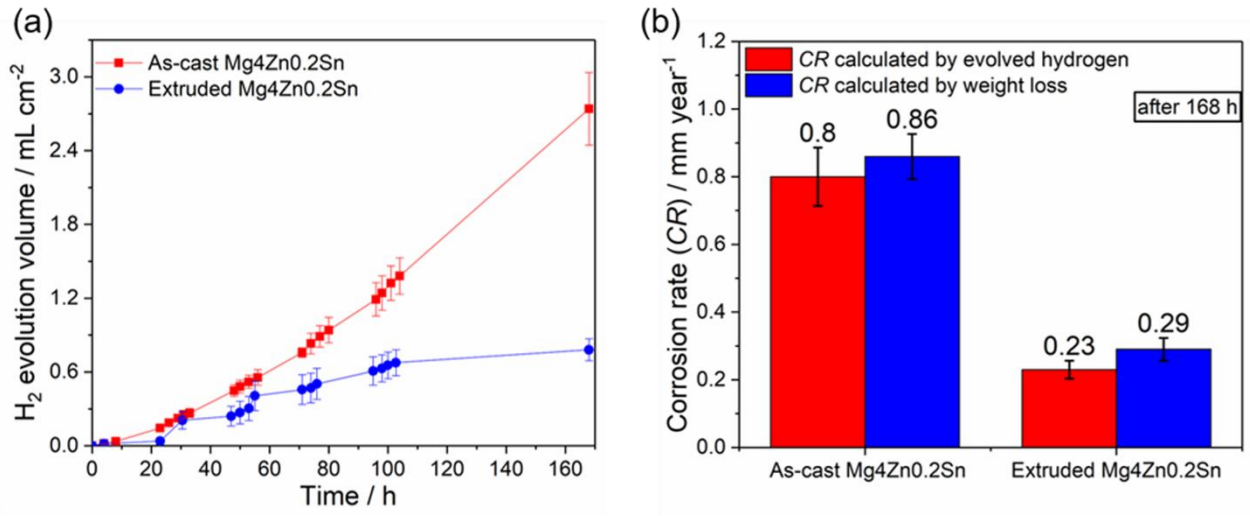
3 **Figure 9**



4

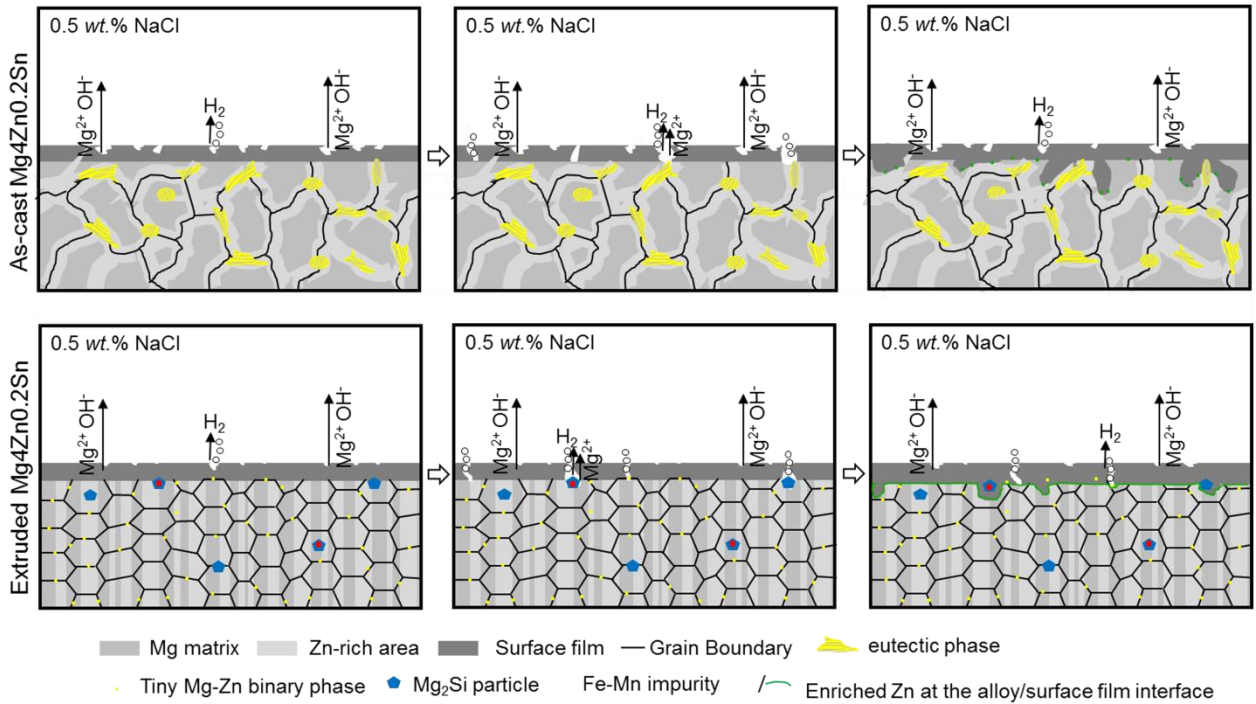
5

1 **Figure 10**



2

3 **Figure 11**



4

5

1 **Tables**

2 **Table 1.** Chemical compositions of as-cast and extruded Mg<sub>4</sub>Zn<sub>0.2</sub>Sn alloys.

Mg <sub>4</sub> Zn <sub>0.2</sub> Sn	Composition (wt.%)							
	Sn	Zn	Fe	Cu	Ni	Mn	Si	Mg
As-cast	0.22	3.92	0.0017	0.0015	0.0007	0.030	0.0133	balance
Extruded	0.17	3.77	0.0018	0.0014	0.0004	0.028	0.0069	balance

3

4 **Table 2.** Chemical compositions for different constituents in the microstructure of as-cast  
5 Mg<sub>4</sub>Zn<sub>0.2</sub>Sn alloy analyzed by EDS.

Element	As-cast Mg <sub>4</sub> Zn <sub>0.2</sub> Sn alloy					
	A-Second phase		B-Brighter particle-free interdendritic region		C-Matrix dendrite	
	at.%	wt.%	at.%	wt.%	at.%	wt.%
Mg	77.9 ± 1.1	56.6 ± 1.6	98.0 ± 0.2	94.7 ± 0.5	99.4 ± 0.1	98.4 ± 0.3
Zn	22.0 ± 1.1	43.1 ± 1.6	1.9 ± 0.2	4.9 ± 0.4	0.5 ± 0.1	1.4 ± 0.3
Sn	0.1 ± 0.0	0.3 ± 0.1	0.1 ± 0.0	0.4 ± 0.0	0.1 ± 0.0	0.2 ± 0.0

6

7 **Table 3.** Chemical compositions for different constituents in the microstructure of extruded  
8 Mg<sub>4</sub>Zn<sub>0.2</sub>Sn alloy analyzed by EDS.

Element	Extruded Mg <sub>4</sub> Zn <sub>0.2</sub> Sn alloy									
	Matrix				F-Tiny particle		Larger particle			
	D-Darker region		E-Brighter region				G-Grey polygonal part/particle		H-Bright globular part	
	at.%	wt.%	at.%	wt.%	at.%	wt.%	at.%	wt.%	at.%	wt.%
Mg	98.8 ± 0.3	96.9 ± 0.7	98.3 ± 0.1	95.6 ± 0.2	98.0 ± 0.1	94.6 ± 0.1	86.2 ± 2.4	80.5 ± 2.7	82.3 ± 1.6	72.9 ± 2.0
Zn	1.1 ± 0.3	2.9 ± 0.7	1.6 ± 0.1	4.2 ± 0.2	2.0 ± 0.0	5.2 ± 0.1	1.1 ± 0.2	2.8 ± 0.5	1.2 ± 0.1	2.9 ± 0.3
Sn	0.1 ± 0.0	0.2 ± 0.0	0.1 ± 0.0	0.2 ± 0.0	0.0 ± 0.0	0.2 ± 0.0	0.8 ± 0.1	3.8 ± 0.6	0.7 ± 0.1	2.8 ± 0.6
Si							11.9 ± 2.5	12.9 ± 2.7	10.6 ± 1.4	10.9 ± 1.4
Mn									1.2 ± 0.1	2.5 ± 0.2
Fe									4.0 ± 0.2	8.0 ± 0.5

9

10

1 **Table 4.** EDS analysis of the constituents in as-cast Mg<sub>4</sub>Zn<sub>0.2</sub>Sn alloy after immersion in 0.5  
 2 wt.% NaCl solution for 6 h followed by the removal of corrosion products.

Element	Matrix		Second phase		Small particles	
	at.%	wt.%	at.%	wt.%	at.%	wt.%
O	1.6	1.0	5.4	2.4	10.5	6.6
Mg	97.4	96.4	63.7	42.3	83.7	79.2
Cr	0.1	0.1	0.4	0.6	0.9	1.8
Zn	0.9	2.3	30.4	54.3	4.8	12.1
Sn	0.0	0.2	0.1	0.4	0.1	0.3

3

4 **Table 5.** Measured and calculated parameters from potentiodynamic polarization curves  
 5 recorded in 0.5 wt.% NaCl solution at room temperature.

6

OCP conditioning time	Alloy	$CR / \text{mm year}^{-1}$	$i_{corr} / \text{mA cm}^{-2}$	$E_{corr} / \text{mV vs. Ag/AgCl}$
30 min	As-cast Mg <sub>4</sub> Zn <sub>0.2</sub> Sn	$0.90 \pm 0.10$	$0.039 \pm 0.004$	$-1556 \pm 6$
	Extruded Mg <sub>4</sub> Zn <sub>0.2</sub> Sn	$2.30 \pm 0.26$	$0.101 \pm 0.010$	$-1536 \pm 4$
48 h	As-cast Mg <sub>4</sub> Zn <sub>0.2</sub> Sn	$1.64 \pm 0.24$	$0.072 \pm 0.010$	$-1496 \pm 12$
	Extruded Mg <sub>4</sub> Zn <sub>0.2</sub> Sn	$0.76 \pm 0.06$	$0.040 \pm 0.002$	$-1443 \pm 25$

7